



HAL
open science

Influence of CO₂ on the Electrical Conductivity and Streaming Potential of Carbonate Rocks

A. Cherubini, Bruno Garcia, Adrian Cerepi, A. Revil

► **To cite this version:**

A. Cherubini, Bruno Garcia, Adrian Cerepi, A. Revil. Influence of CO₂ on the Electrical Conductivity and Streaming Potential of Carbonate Rocks. *Journal of Geophysical Research: Solid Earth*, 2019, 124 (10), pp.10056-10073. 10.1029/2018JB017057 . hal-02324326

HAL Id: hal-02324326

<https://hal.science/hal-02324326v1>



Submitted on 3 Feb 2020

HAL is a multi-disciplinary open access archive for the deposit and dissemination of scientific research documents, whether they are published or not. The documents may come from teaching and research institutions in France or abroad, or from public or private research centers.

L'archive ouverte pluridisciplinaire **HAL**, est destinée au dépôt et à la diffusion de documents scientifiques de niveau recherche, publiés ou non, émanant des établissements d'enseignement et de recherche français ou étrangers, des laboratoires publics ou privés.

RESEARCH ARTICLE

10.1029/2018JB017057

Influence of CO₂ on the Electrical Conductivity and Streaming Potential of Carbonate RocksA. Cherubini^{1,2} , B. Garcia¹, A. Cerepi², and A. Revil³ ¹Geosciences Division, GeoFluids and Rocks Department, IFP Energies Nouvelles, Rueil-Malmaison, France, ²EA 4592 'Géorressources et Environnement', ENSEGD-Bordeaux INP, Pessac, France, ³Université Grenoble Alpes, Université Savoie Mont Blanc, CNRS, IRD, IFSTTAR, ISTERRE, Grenoble, France

Key Points:

- The dissolution of calcite leads to a decrease of the magnitude of the streaming potential coupling coefficient
- The pore water conductivity is dominated by the calcite dissolution in carbonates
- Calcite dissolution rates calculated from streaming potential measurements are consistent with PHREEQC simulations

Correspondence to:

A. Cherubini,
aurelien.cherubini@gmail.com

Citation:

Cherubini, A., Garcia, B., Cerepi, A., & Revil, A. (2019). Influence of CO₂ on the electrical conductivity and streaming potential of carbonate rocks. *Journal of Geophysical Research: Solid Earth*, 124. <https://doi.org/10.1029/2018JB017057>

Received 19 NOV 2018

Accepted 22 AUG 2019

Accepted article online 29 AUG 2019

Abstract Minimally intrusive geophysical methods are required to monitor CO₂ leakages from underground storage reservoirs. We investigate the impact of gaseous CO₂ on both electrical conductivity and electrokinetic properties of two limestones during their drainage. These data are contrasted with measurements performed on one clay-free sandstone. The initial NaCl brine concentrations before drainage (from 8.5 to 17.1 mMol/L) correspond to the limit between freshwater and slightly brackish water. These values are representative to saturated brine formations inside which CO₂ can be stored. Using these water salinities, the surface conductivity of the samples represents less than 5% of the overall electrical conductivity. A CO₂ release leads to an increase of the electrical conductivity of the rock during drainage in limestones and no change in sandstone. This increase in the electrical conductivity is due to the dissolution of calcite with the concomitant release of Ca²⁺ and HCO₃⁻ in the pore water. It is not due to the CO₂ dissociation in the pore water in the pore pressure range 0–0.5 MPa and at a temperature of $T = 20$ °C. The measurements of the streaming potential show a substantial decrease of the streaming potential coupling coefficient and zeta potential magnitudes after a CO₂ release in carbonates. This observation is explained by the increase of the ionic strength of the pore water in the course of the experiment. This change can be used, in turn, to determine calcite dissolution rates from the measurement of the electrokinetic properties.

1. Introduction

Geological CO₂ sequestration is considered as a viable way of reducing CO₂ concentration into the atmosphere (Benson & Cole, 2008; Moore et al., 2004). In order to host CO₂, underground locations have been proposed such as depleted oil and gas reservoirs (Jenkins et al., 2012), saturated brine formations (Benson & Cole, 2008), and coal seams (Shi & Durucan, 2005). The injected CO₂ is generally trapped below low-permeability and high capillary entry pressure seals corresponding for instance to clay-rich anticlines (Liu et al., 2011). CO₂ dissolves partly into the pore water and interacts with the surrounding minerals promoting dissolution/precipitation reactions (Bachu et al., 1994). Two well-known geophysical galvanometric methods can be used to monitor fluid flow in shallow or deep formations, namely, the self-potential (SP) method and the electrical conductivity/resistivity tomography methods (Le Roux et al., 2013; Zhou et al., 2012).

The electrical conductivity method is an active geophysical method. A low-frequency current is injected in the ground and the resulting field is recorded in order to reconstruct the conductivity/resistivity distribution of the subsurface. This method is already used in the field to identify CO₂ leakages (Le Roux et al., 2013; Zhou et al., 2012). Recent studies showed the ability of electrical conductivity monitoring to detect variations caused by CO₂ flowing in porous media (Giese et al., 2009; Kiessling et al., 2010; Schmidt-Hattenberge et al., 2011; Strazisar et al., 2009; Würdemann et al., 2010; Zhou et al., 2012). Strazisar et al. (2009) showed, for instance, the increase of the size of a conductivity anomaly observed after the injection of CO₂ in a vertical injection well. They suggested that the dissolution of CO₂ in the pore water is responsible for such a conductivity increase. Along the same line, Lewicki et al. (2007) argued that only a small amount of CO₂ is dissolved in the pore water system during its release, leading only to a slight pore water conductivity increase. This increase is due to the CO₂ dissociation in pore water, leading to an increase of the ionic strength of the solution. Recently, some authors focused on the carbonate/CO₂ interactions to explain the observations mentioned above (e.g., Cohen et al., 2013; Garcia et al., 2013; Loisy et al., 2013). The conductivity of the pore water decreases when the water saturation decreases. However, there is also two other effects impacting

the conductivity of the rock mixture, namely, (a) the CO₂ dissociation in water and (b) the carbonate dissolution. These two additional effects can counterbalance the saturation effect, leading to an increase of the conductivity of the mixture (Le Roux et al., 2013).

The self-potential method is a passive galvanometric technique consisting in recording the electrical field associated with in situ sources of electrical current in the subsurface. Such current source densities can be, for instance, associated with the flow of the liquid water phase in a porous material. Such component is said to be of electrokinetic nature (Aubert & Y  n   Atanga, 1996; Darnet et al., 2003; Jougnot et al., 2012; Naudet et al., 2003; Naudet et al., 2004). The resulting electrical current density is called the streaming current. The self-potential method is a well-recognized method in geophysics used to identify fluid flow characteristics such as preferential flow paths (Corwin & Hoover, 1979; Revil et al., 2004) or transport properties including permeability and the specific storage coefficient (Cerepi et al., 2017; Cherubini et al., 2018; Jackson, 2010; Perrier & Morat, 2000; Revil et al., 2007; Soueid Ahmed et al., 2016). Streaming potential signals are due to the presence of an electrical diffuse layer on the surface of the minerals (Dukhin & Derjaguin, 1974; Overbeek, 1952). The drag of the excess of charge of the diffuse layer by the flow of the pore water generates the streaming current. This current serves as a source to generate electromagnetic signals, which can be measured remotely.

Our goal in this study is to develop experiments showing how electrical conductivity and electrokinetic properties are influenced by a release of CO₂ in carbonate rocks. We use two limestones known to be reactive in presence of CO₂. These data will be contrasted with similar experiments realized with a sandstone core sample. We use a clean silica-based Fontainebleau sandstone for these additional experiments. Regarding the potential influence of gaseous CO₂ on the electrical conductivity, we want to test the two different assumptions proposed in the literature and briefly discussed above, that is, (i) the dissociation of CO₂ in the pore water can control the pore water conductivity (see Dreybrodt et al., 1997; Lide, 2003) and (ii) calcite dissolution can change the ionic strength of the pore water. We propose a model allowing us to quantify calcite dissolution rates with the self-potential method, using the streaming potential coupling coefficient as a tool to define these rates.

2. Theory

2.1. Electrical Conductivity

The electrical conductivity σ of rocks is the sum of two contributions, (i) one contribution through the bulk pore space and dependent on the conductivity of the pore water σ_w , plus (ii) a second contribution called surface conductivity and written below as σ_s . This second contribution is dispersive (i.e., frequency dependent) and related to the conduction in the electrical double layer (Stern and Gouy-Chapman diffuse layers) coating the surface of the minerals. We use the following conductivity equation defining the surface conductivity σ_s ,

$$\sigma = \frac{1}{F} \sigma_w + \sigma_s, \quad (1)$$

where F denotes the intrinsic formation factor (dimensionless) and is connected to the porosity ϕ (dimensionless) by the first Archie's law (Archie, 1942),

$$F = \phi^{-m}. \quad (2)$$

In equation (2), m is called the cementation or porosity exponent.

According to Waxman and Smits (1968), the effect of saturation S_w on electrical conductivity is given by

$$\sigma = S_w^n \frac{1}{F} \sigma_w + S_w^{n-1} \sigma_s, \quad (3)$$

where n (-) represents the saturation or second Archie's exponent. The resistivity index is defined as the ratio of the conductivity at full saturation (σ_0) and the conductivity at a given saturation (σ). The resistivity index RI (-) is therefore given by (Revil et al., 2014)

$$RI = S_w^{-n} \left(\frac{\sigma_w + F\sigma_s}{\sigma_w + F\sigma_s/S_w} \right). \quad (4)$$

When surface conductivity can be neglected compared to bulk water conductivity, the resistivity index can be written as

$$\lim_{\sigma_s \rightarrow 0} RI = S_w^{-n}, \quad (5)$$

and under the same assumption F can be approximated as the ratio of the pore water conductivity (σ_w) to the conductivity of the sample at full saturation (σ_0) as

$$\lim_{\sigma_s \rightarrow 0} F = \frac{\sigma_w}{\sigma_0}, \quad (6)$$

In the case of a gaseous CO_2 injection, the presence of CO_2 impacts the saturation S_w . Since CO_2 is not an immiscible gas, it will also impact the conductivity of the pore water solution through the dissolution of the carbonic acid in the pore water and the potential dissolution of the mineral into water. In this case, Le Roux et al. (2013) formulated the resistivity index (RI_{CO_2}) in terms of the pore water conductivity before CO_2 release (σ_w) and pore water conductivity at CO_2 saturation ($\sigma_{w-\text{CO}_2}$) assuming that m , n , and ϕ are constant under CO_2 or N_2 conditions,

$$\lim_{\sigma_s \rightarrow 0} RI_{\text{CO}_2} = \frac{\sigma_w}{\sigma_{w-\text{CO}_2}} S_w^{-n}. \quad (7)$$

2.2. Streaming Potential

There are two types of electrical current in porous media in which pore water flows. The first current is the classical conduction current and is due to the fluxes of charges under the effect of the electrical field. The second current is a source current associated with the drag of the electrical charges by the flow of the pore water itself. This advective current is called the streaming current. The total current density is the sum of the two current densities. For the case of a rock sample crossed by fluid flow and acting as an open system, the total current density is equal to zero and that the streaming current density counterbalances the conduction current density. In this case, the streaming potential $\Delta\psi$ (V) is given by (e.g., Revil et al., 2007)

$$\Delta\Psi = \frac{\varepsilon_w \zeta}{\eta_w F \left(\frac{\sigma_w}{F} + \sigma_s \right)} \Delta p. \quad (8)$$

where ε_w (F/m) denotes the dielectric permittivity of the liquid pore water, ζ (V) the zeta potential (the potential of the diffuse layer at the shear plane close to the mineral surface where the velocity of the pore water is zero), η_w (Pa s) the dynamic viscosity of the liquid water phase, ψ (V) the electrical potential of electrokinetic nature and measured on the end faces of the rock sample, and p (Pa) the pore fluid pressure. If the surface conductivity is neglected, the streaming potential reduces to

$$\lim_{\sigma_s \rightarrow 0} \Delta\Psi = \frac{\varepsilon_w \zeta}{\eta_w \sigma_w} \Delta p. \quad (9)$$

The streaming potential coupling coefficient $C(S_w)$ (V/Pa) is given by (Helmholtz, 1879),

$$C(S_w) = \left(\frac{\Delta\Psi}{\Delta p} \right)_{J=0}. \quad (10)$$

The zeta potential is related to the streaming potential coupling coefficient (e.g., Alroudhani et al., 2016; Guichet et al., 2006; Li et al., 2016; Revil et al., 1999) using the intrinsic formation factor, F , as

Table 1
Petrophysical Characteristics of the Limestones (L1 and L2) and the Sandstone (S1) Samples Studied

Sample	ϕ_w	k (mD)	F	m	n			σ_s (S/m)
					N ₂	CO ₂	N _w	
L1	0.28	80	16.7	2.21	2.47	2.12	4.5	7.0×10^{-4}
L2	0.27	100	16.7	2.15	2.30	2.62	4.5	7.0×10^{-4}
S1	0.13	130	51.6	1.93	2.87	3.04	4.6	1.1×10^{-4} a

Note. The parameters ϕ and k are respectively the porosity and the permeability. F is the formation factor, m , n , and N_w are respectively the cementation, saturation, and Corey exponents; σ_s is the surface conductivity.

^aData calculated from the formula of Revil et al. (2014) for the Fontainebleau sandstones $\log \sigma_s = -3.11 - \log(F\phi)$.

$$C_{\text{sat}} = \frac{\varepsilon_w \zeta}{\eta_w F \sigma}, \quad (11)$$

and can be reduced to the well-known Helmholtz-Smoluchowski equation if we neglect the surface conductivity (e.g., Hunter, 1981),

$$\lim_{\sigma_s \rightarrow 0} C_{\text{sat}} = \frac{\varepsilon_w \zeta}{\eta_w \sigma_w}. \quad (12)$$

According to Linde et al. (2007) and Revil et al. (2007), the streaming potential coupling coefficient can also be related to the dynamic excess of charge dragged by the electrolyte \widehat{Q}_V (given by a volume average of the local current density given by the local charge density of the diffuse layer times the local fluid flow velocity) and the permeability k , as

$$C_{\text{sat}} = -\frac{k \widehat{Q}_V}{\eta_w \sigma}. \quad (13)$$

The relative streaming potential coupling coefficient is given by the ratio of the coupling coefficient at saturation S_w to the value of the coupling coefficient at full saturation (Revil & Cerepi, 2004),

$$C_r(S_w) = \frac{C(S_w)}{C_{\text{sat}}}. \quad (14)$$

Revil et al. (2007) proposed a relationship tested in Cerepi et al. (2017) and Cherubini et al. (2018) with nitrogen between the relative streaming potential coupling coefficient C_r (-) and the saturation S_w (-) using the Corey exponent (N_w) defined using relative permeability curves according to Brooks and Corey (1964), and the saturation Archie's exponent (n) as

$$C_r(S_w) = \frac{1}{S_w^{n+1}} (S_e)^{N_w}, \quad (15)$$

with

$$S_e = \left(\frac{S_w - S_{wi}}{1 - S_{wi}} \right), \quad (16)$$

where S_{wi} and S_e denote the irreducible water saturation and the effective saturation, respectively.

3. Experimental Methodology

3.1. Core Samples

Three core samples were investigated at full and partial brine saturation. They include two algal rhodolith packstones (L1 and L2, also called Estailades limestones) from Provence (southeast of France) and one clay-free sandstone (S1). This clay-free sandstone corresponds to a Fontainebleau sandstone from the Paris basin. This pure silica sandstone is considered much less reactive (if not reactive at all) with respect to CO₂. The three core samples have a length of 80 mm and a cross-section diameter of 39 mm. They were drilled parallel to the stratification using a drilling tool made with tungsten carbide to avoid fracturing the samples. They were dried in an oven (60 °C) before each experiment and then saturated with a degassed brine using a vacuum pump (5 Pa). We checked that the drilling operation does not create any fractures using a micro scanner (CT-Scan). Samples L1 and L2 were drilled in the same block, few centimeters from each other.

The petrophysical properties of the core samples are reported in Table 1. The connected porosity is calculated using the dry mass difference method ($\phi_w = V_V/V_T$, where V_V (m³) and V_T (m³) are the volume of the connected voids in the sample and the total volume of the sample, respectively). The quantity V_V is

calculated from the mass difference between saturated and dry samples, using a pore water density equal to 1.0 g/cm^3 . We obtained $\phi_w = 0.28$, $\phi_w = 0.27$, and $\phi_w = 0.13$ for the samples L1, L2, and S1, respectively. For the sample L1, we also calculated the porosity using a scanner, considering all the voids of the sample (connected and disconnected voids). We obtain $\phi_{\text{scan}} = 0.29$ that is slightly higher than the value calculated using the dry mass difference method ($\phi_w = 0.28$). This slight difference could be explained by a minor presence of disconnected porosity ($\phi_{\text{disconnected}} \approx 0.01$). The permeability (k , in square meters) at brine saturation is determined by measuring the pressure difference measured for each brine rate, using the Darcy's law, when steady state is reached. The saturation Archie's exponent (n) is calculated using equation (5) using conductivity data at different saturations. The cementation exponent (m) is calculated using the first Archie's law (equation (2)) using the porosity and formation factor data. Finally, the Corey exponent (N_w) is determined by fitting relative permeability data with the Brooks and Corey (1964) model.

3.2. Apparatus and Experimental Procedure

The experimental setup used to measure the streaming potential coupling coefficient and the conductivity of the samples is shown in Figure 1. The cylindrical core samples are wrapped in a rubber sleeve and confined within a core holder with a confining pressure equal to 3 MPa. We proceeded to some tests of fluid flow with a scanner to control fluid paths in real time. With the confinement pressure of 3 MPa, the pore fluid flows through the core sample and is not expected to flow through the sample-sleeve interface. The confining pressure is regulated by a pump to avoid pressure fluctuations due to temperature variations and possible leakages and is constant throughout the experiment. The stainless steel body of the core holder does not come into contact with the sample or fluids (except the oil confinement) and is grounded.

The electrical measurements (streaming potential and electrical conductivity experiments) as well as the relative permeability measurements are performed using a steady-state flooding technique. Such a system simultaneously allows injecting both a NaCl brine prepared by mixing pure dehydrated NaCl with deionized water (through the two inlets shown in Figure 1) with flow rates between 0.1 and 20 ml/min and gas (one inlet in the center of the spiral injection, Figure 1) in the sample (rocks are water wet). For each drainage experiment on the samples L1, L2, and S1, the gas partial pressure (N_2 or CO_2) is in the range 0.1–0.4 MPa. Brine and gas are therefore mixed when entering the rock sample. The steady state is reached when the pressure difference (Δp) between the inlet and the outlet of the sample is stable, after few minutes. The spirals are also used as electrodes to measure the conductivity of the core sample and the streaming potential coupling coefficient. These electrodes are made of hastelloy, a material highly resistant to corrosion.

One pump is used to inject brine in the core at constant flow rate, while a gas flow regulator (Bronkorst F-201-CV) regulates the flow of gas. The brine/gas flow rate ratio is decreasing during the drainage phase. The pressure difference measured for each brine-gas ratio permits to measure relative permeabilities using Darcy's law when steady state is reached and when the water saturation in the sample is stable. At each saturation, the electrical conductivity of the sample and the streaming potential coupling coefficient are measured. Concerning electrical conductivity measurements, the voltage is self-regulated by the impedance meter in the range 0–3 V, with a phase error less than 1 mrad. Measurements are performed with a Solartron 1265 at 1 kHz, using a four-electrode arrangement, separating the current and voltage electrodes. Current electrodes are 8 cm apart, while voltage electrodes are separated by 2.5 cm.

As we calculate the pore water conductivity using the model of Le Roux et al. (2013), it is necessary to verify if the porosity remains the same, before and after a CO_2 injection. If not, Le Roux et al. (2013) model corresponding to equation (7) is not valid in our case. The sample L1 was investigated using the computerized tomography method (Figure 2). The X-ray absorption was calculated in the full saturated sample before CO_2 release (red line, Figure 2a) and after drainage, when the sample is saturated again (blue line, Figure 2a).

4. Results and Discussion

4.1. CO_2 Effects on Porosity During Drainage

A drainage experiment using gaseous CO_2 was led on the sample L2, at ambient temperature (20 °C). The pore water pressure before drainage is around 0.15 MPa (the water flow rate is equal to 10 ml/min), and CO_2

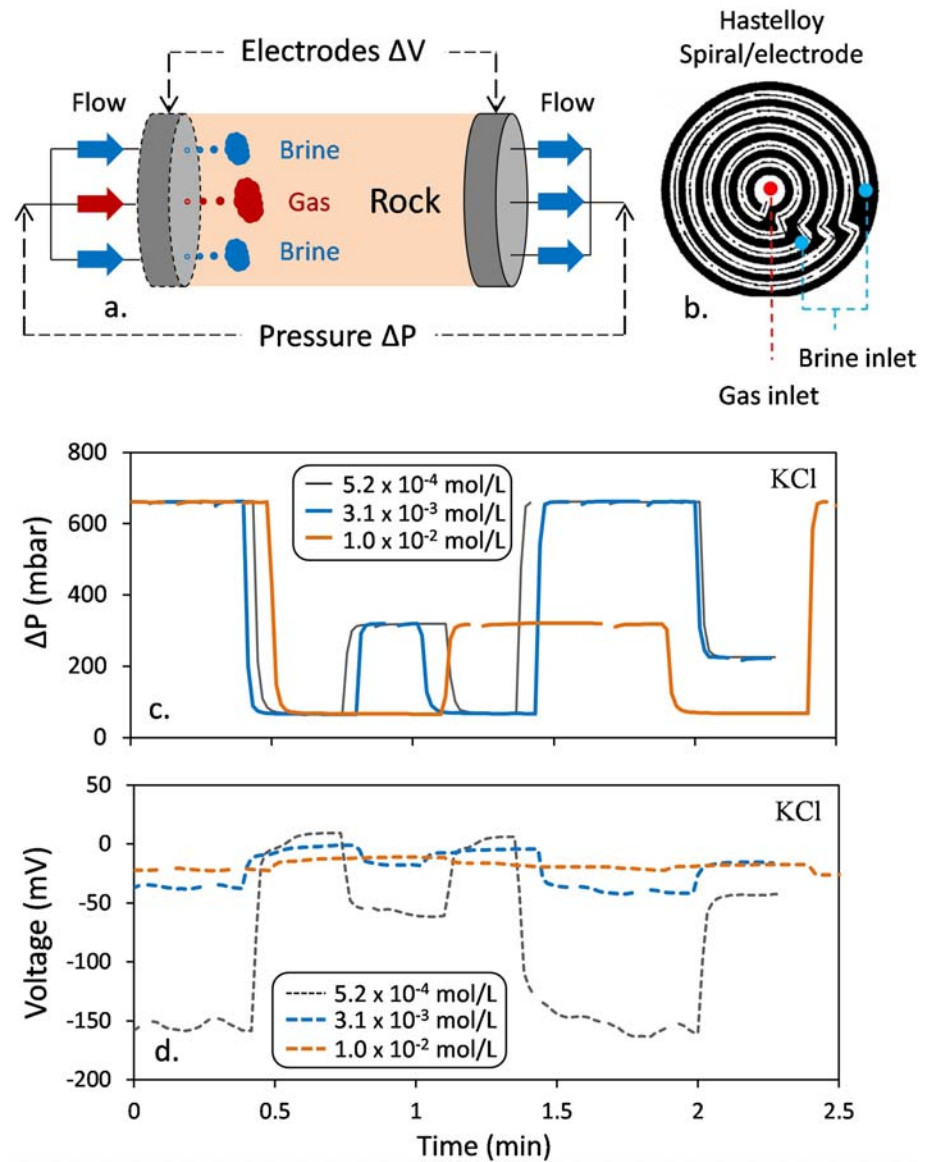


Figure 1. Sketch of the experimental setup used to measure the streaming potential coupling coefficient and electrical conductivity of the porous plug. (a) Positioning of the electrodes (gray circles). (b) Sketch of the nonpolarizable Hastelloy electrodes used to measure the streaming potential and the sample electrical conductivity at 1 kHz. The electrode has the same diameter as the cylindrical core sample wrapped in the sleeve. At the same time, the shape of the electrodes allow the simultaneous injection of both the gas and brine in the core sample. (c) The streaming potential coupling coefficient is calculated using the ratio of the pressure difference between the inlet and the outlet of the sample the voltage difference. (d) Streaming voltage difference across the core sample. We use a KCl brine at three different salinities (5.2×10^{-4} ; 3.1×10^{-3} ; 1.0×10^{-2} Mol/L) on the sample L1.

partial pressures (in MPa) are in the range $0.1 < p_{CO_2} < 0.4$ during drainage. When the irreducible water saturation is reached, the sample is saturated again using the same brine. The CT number difference (which is a normalized value of the X-ray absorption coefficient of a pixel) has a positive value along the core (Figure 2b), meaning that the density of the sample-brine system was higher before drainage. We also note that the effective dissolution is higher close to the inlet and is almost equal to zero near the outlet. The system brine- CO_2 -dissolved ions tend toward chemical equilibrium as the CO_2 flows in the sample. This observation is consistent with the studies by both Grigg et al. (2003) and Luquot and Gouze (2009).

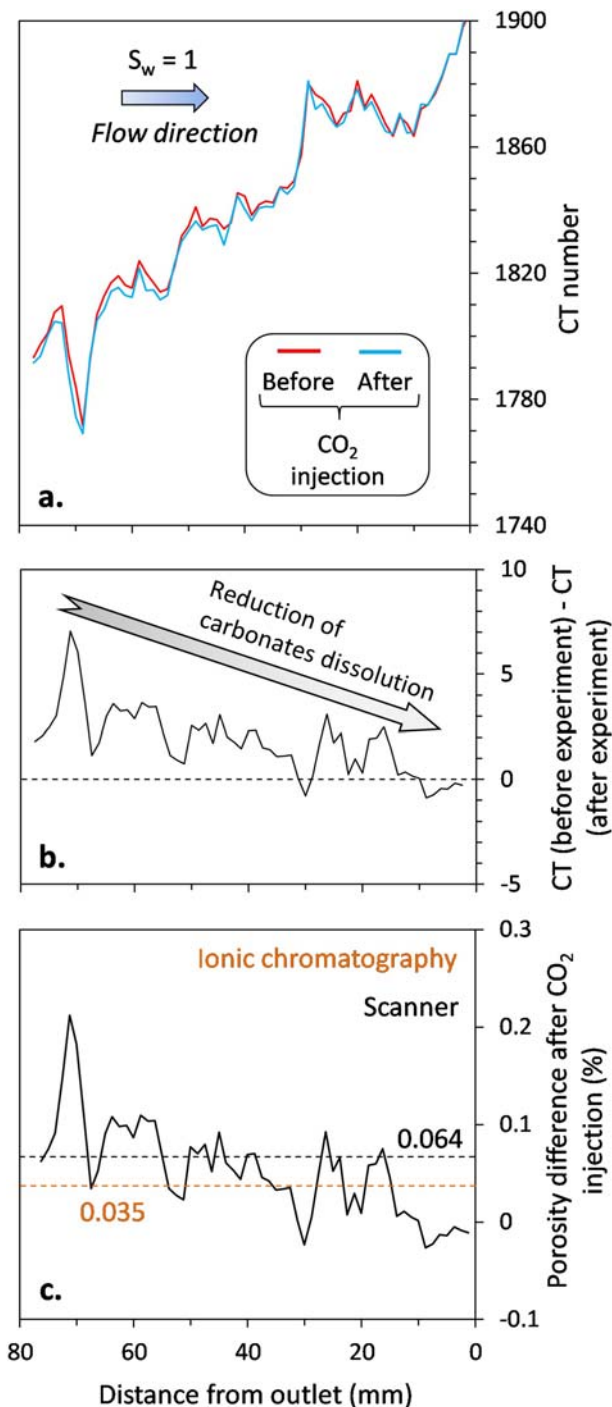


Figure 2. Computed tomography scan response of the sample L1 under N_2 and CO_2 conditions. (a) CT-scan along the core sample L1 before drainage by CO_2 (red line) and after CO_2 injection (blue line). These test are performed at full brine saturation ($[NaCl] = 0.017$ Mol/L). (b) Difference between the CT numbers showing higher values in the vicinity of the inlet. Note that the difference tends to zero at the outlet of the sample. This implies in turn an increase of porosity in the vicinity of the inlet. (c) Generated porosity after the drainage phase using CO_2 .

With the scanner laboratory team, we first establish a CT number baseline using the sample saturated by deionized water. Then, we remove the sample of the sleeve to dry it in an oven (at $60^\circ C$). We replace the dry sample in the sleeve and establish another baseline of the CT number. In each case (saturated or dry state), the sleeve is in the stainless steel body to consider the X-ray attenuation due to the body composition. Knowing the CT numbers of saturated and dry samples, and the densities of the water and the samples, we are able to define a calibration curve allowing us to convert the CT number to porosity (Figure 2c). The result shows that the increase of porosity during the drainage process is negligible. Indeed, the average of absolute porosity variation along the core is only equal to $+0.06\%$. In comparison, the dissolved material balance calculated using ionic chromatography gives an absolute porosity variation equal to $+0.035\%$, that is in the same range. We also noted that the dissolution is higher close to the inlet (porosity increase of $+0.2\%$) than to the outlet of the sample (no porosity variation). However, we could not compare these results with respect to the porosity calculated using the dry mass difference before and after experiment. Indeed, we observe a disaggregation of the sample during the removal process from the sleeve.

Other authors found porosity variations much higher than our values (Auffray et al., 2016), between $+5\%$ and $+15\%$ for gaseous CO_2 partial pressures between 3 and 9 MPa. The solubility of CO_2 is pressure, temperature, and ionic strength dependent. According to the Henry law in a CO_2/H_2O system, the solubility of CO_2 in water decreases when the temperature increases up to $150^\circ C$ under atmospheric pressure (Enick & Klara, 1990) and increases for temperatures higher than $150^\circ C$. On the other hand, the aqueous solubility of CO_2 is greater at elevated pressure (Rosenbauer et al., 2005), which may explain the high dissolution rate of calcite in the study of Auffray et al. (2016).

4.2. Influence of CO_2 on the Conductivity

4.2.1. Surface Conductivity

In order to determine if the surface conductivity can be neglected, we performed electrical conductivity measurements on the three core samples at different pore water conductivities (Figure 3). We see for all samples the high-salinity asymptotic behavior (equation (6)) for which the pore water conductivity dominates (from $\sigma_w/F = 1.4 \times 10^{-2}$ S/m for the limestones L1 and L2 and $\sigma_w/F = 2.2 \times 10^{-3}$ S/m for the sandstone S1) and the low-salinity behavior for which surface conductivity dominates. Then, the surface conductivity for the limestones is equal to $\sigma_s = 7.0 \times 10^{-4}$ S/m. For the Fontainebleau sandstone, the surface conductivity has been calculated following the formula $\log \sigma_s = -3.11 - \log(F\phi)$ given in Revil et al. (2014) and validated for a large data set of Fontainebleau sandstones, using the formation factor and the porosity. The surface conductivity is equal to $\sigma_s = 1.1 \times 10^{-4}$ S/m. In each case, $\sigma_s \ll \sigma_w/F$ and the surface conductivity can be neglected with respect to the pore water conductivity. The intrinsic formation factor is equal to 11.9 for the two limestones and 51.6 for the sandstone.

4.2.2. Second Archie's Exponent in a Brine-Gas System

The electrical conductivity of two samples (one pure limestone, L1, and one sandstone, S1) was measured during a drainage process. We used these two types of rocks with the goal of determining the influence of CO_2 on the rock conductivity in presence of carbonates. In contrast,

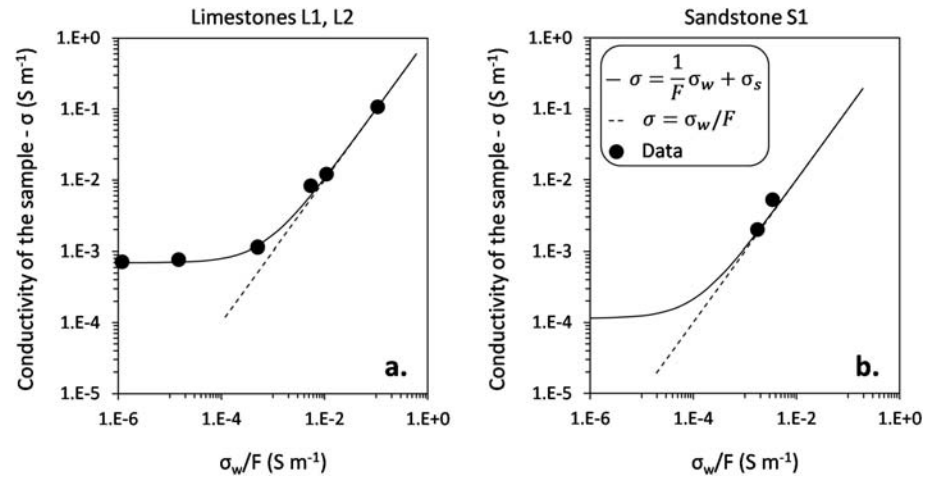


Figure 3. Conductivity of the samples versus pore water conductivity σ_w at full saturation. The data (black circles) are fitted with the conductivity model (plain line) of Waxman and Smits (1968). The surface conductivity σ_s is equal to (a) 7.0×10^{-4} S/m in the limestones L1 and L2 and (b) 1.1×10^{-4} S/m in the sandstone S1. For the sandstone, σ_s is calculated using the formula $\log \sigma_s = -3.11 - \log(F\phi)$ from Revil et al. (2014) due to the lack of data at low salinities.

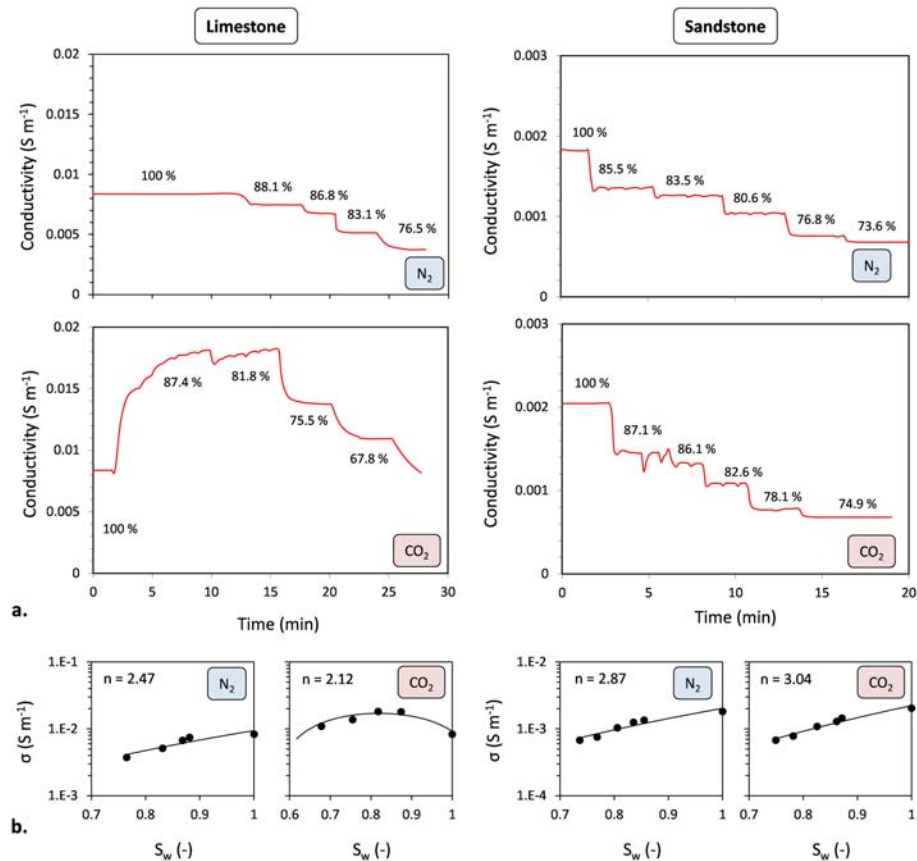


Figure 4. Conductivity during drainage under N_2 and CO_2 conditions (a) in the limestone L1 (left column) and the sandstone S1 (right column). (b) When N_2 is injected, the conductivity follows equation (5) in both rocks (surface conductivity can be neglected), while it is not the case in the presence of CO_2 for the limestone (the pore fluid conductivity has to be corrected). The brine is composed of 8.55 mMol/L NaCl ($\sigma_w = 1.0 \times 10^{-1}$ S/m at 20 °C) in each case.

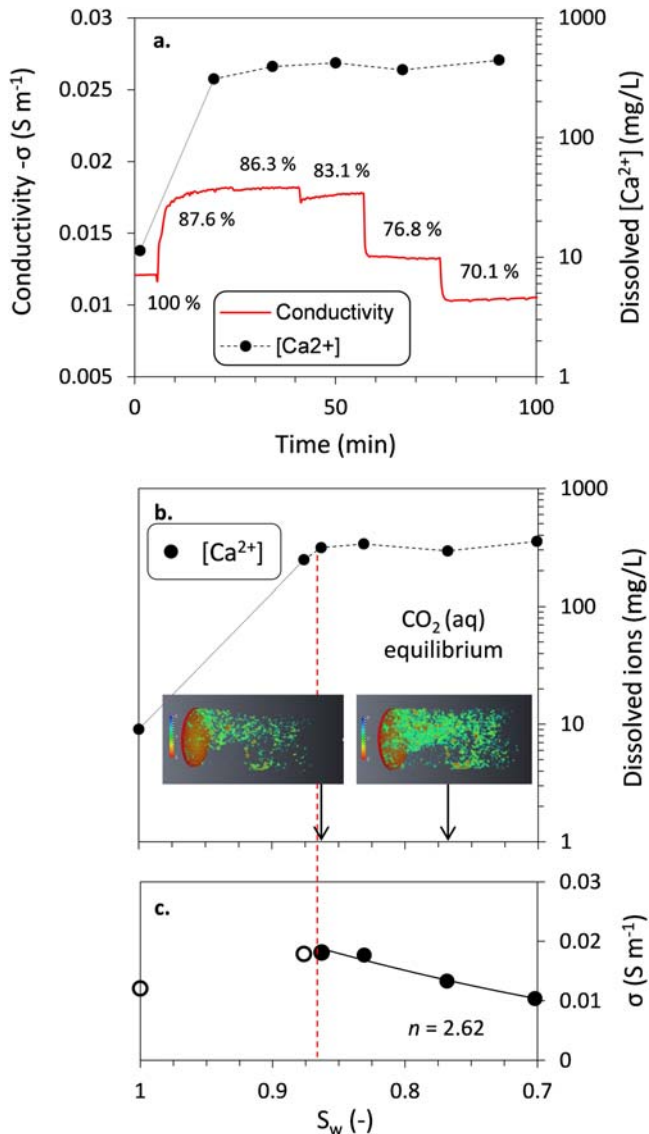
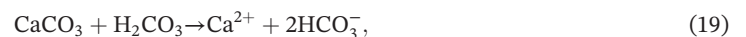


Figure 5. Influence of calcite dissolution on the conductivity during drainage under CO_2 conditions. (a) Conductivity of the sample L2 during the drainage phase, with a brine concentration equal to 17.1 mMol/L before CO_2 injection, associated with (b) calcite dissolution into the pore water for each saturation step. Two tomograms show the gas phase (green bubbles) for two water saturation steps (0.863 and 0.768). CO_2 equilibrium is reached at the first drainage step ($S_w = 0.876$), allowing to calculate (c) the saturation Archie's exponent ($n = 2.62$).

4.2.3. Calcite Dissolution in a Brine- CO_2 System

A drainage experiment in carbonate using CO_2 has been performed with sample L2 with an initial NaCl concentration equal to 0.017 Mol/L. From equation (17), the formation of H_2CO_3 and H^+ leads to chemical reactions responsible for the dissolution of calcite (Talman et al., 1990)



silica materials are not expected to react in presence of CO_2 . In the general case, if the gas does not react with the sample, the electrical conductivity of the core sample decreases when the water saturation decreases too. Both drainage experiments were first performed using nitrogen acting as neutral gas (Figure 4a, upper line). Then, these drainage experiments were performed again using carbon dioxide (Figure 4a, lower line). In all these experiments, the salinity of the pore water is equal to 8.55 mMol/L of NaCl ($\sigma_w = 1.0 \times 10^{-1}$ S/m at 20 °C) in each case. As expected, the rock conductivity and the water saturation are related to each other by a power law (equation (5)) under nitrogen conditions (Archie, 1942). Equation (5) is indeed valid in this case since as shown in section 4.2, the surface conductivity can be safely neglected for the salinity used in our experiment. We obtain $n = 2.47$ and $n = 2.87$ for the core samples L1 and S1, respectively (Figure 4b). Under carbon dioxide conditions, $n = 3.04$ for S1, while n cannot be directly estimated for L1 without pore water conductivity corrections, due to the conductivity increase during the first part of drainage (between $S_w = 1$ and $S_w = 0.818$). The same phenomenon was previously observed in Le Roux et al. (2013). A significant increase of conductivity is observed in this case when carbon dioxide is injected in carbonate rocks (Figure 4a, lower left corner) due to the elevation of the ionic strength of the electrolyte (between 0 and 15min of injection). The unexpected peaks (Figure 4a, lower right corner) during the first step of the CO_2 release (at $S_w = 0.871$) could be due to the heterogeneity of the mixture close to the electrodes area. The gaseous CO_2 does not seem to have finished migrating by gravity to the top of the sample.

This conductivity increase can be associated with a change in the pore water conductivity related to CO_2 dissolution (Lindsay, 1979; Plummer et al., 1979; Rasmuson et al., 1990). The dissolution of CO_2 in the pore water can be written as



These ionic species (bicarbonate and carbonate) influence the pore water conductivity in a given set of conditions and, thereby, the electrical rock conductivity. This reaction holds also in sandstones. However, in the same experimental conditions (temperature and pore pressure), the electrical rock conductivity during drainage has the same trend in the sandstone S1 using N_2 or CO_2 . From these observations, we expect that the dissociation of CO_2 in pore water cannot be the mechanism controlling the electrical rock conductivity change in carbonates. Next, we investigate the influence of the dissolution of calcite regarding the observed change in the electrical conductivity.

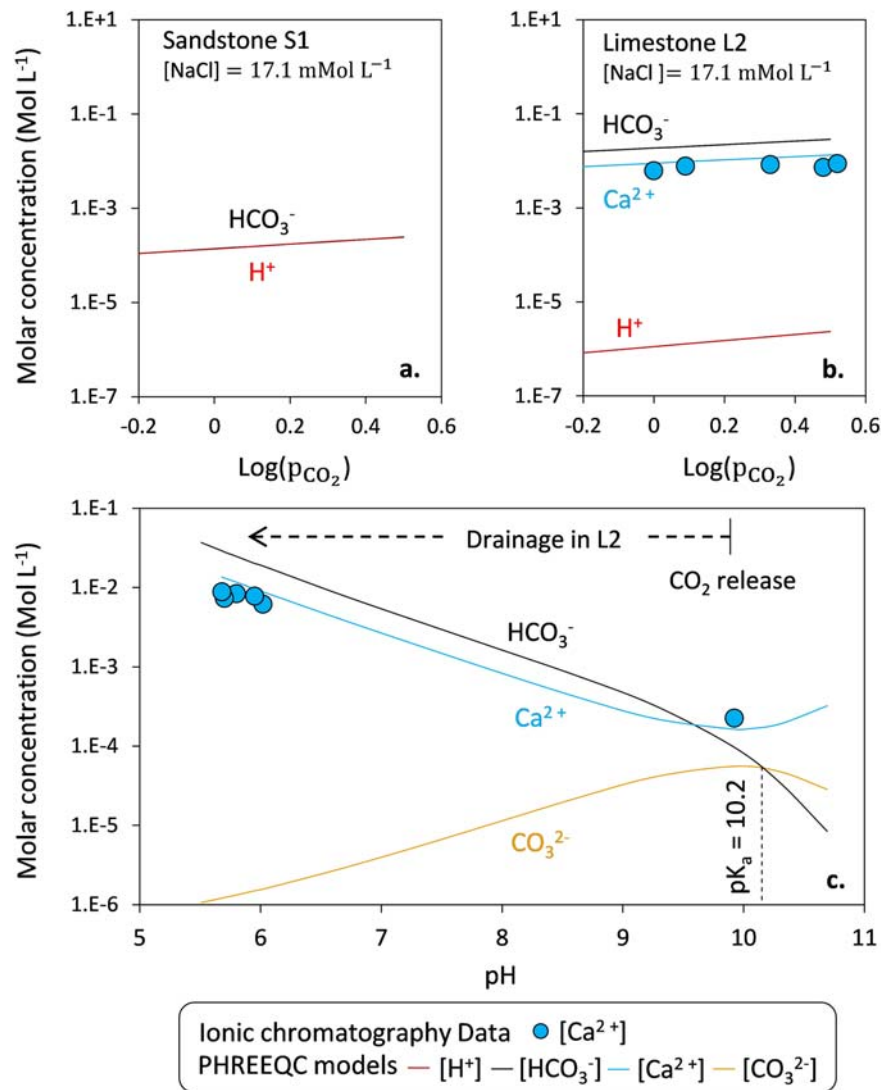


Figure 6. Simulated Molar concentration (using PHREEQC) of dissolved ions versus CO₂ partial pressure during drainage. (a) Simulation for sandstone S1, following the reaction $\text{CO}_2 + \text{H}_2\text{O} \leftrightarrow \text{H}^+ + \text{HCO}_3^-$ (b) Simulation for limestone L2 following the global reaction $\text{CaCO}_3 + \text{H}_2\text{O} + \text{CO}_2 \rightarrow \text{Ca}^{2+} + 2\text{HCO}_3^-$. (c) The model fits very well with data of dissolved Ca²⁺ (blue circles) measured using ionic chromatography and predicts a drastic decrease of CO₃²⁻ during drainage and an increase of Ca²⁺ and HCO₃⁻ due to the decrease of the pH.

Although H⁺, H₂CO₃, and H₂O reaction with calcite occur simultaneously throughout (far from equilibrium, as well as at equilibrium), the calcite dissolution is dominated by reaction with single species as a function of pH and CO₂ partial pressure (Plummer et al., 1979). The reaction of calcite with water is not considered in our dissolution rate, because it occurs when $p_{\text{CO}_2} \leq 0.01$ MPa (Plummer et al., 1979), which is significantly lower than the CO₂ partial pressure in our system. Moreover, we consider that there is no longer CO₂ in the brine (liquid or supercritical) when the system reaches the equilibrium due to temperature (20 °C) and pressure (<0.5 MPa) conditions. Then, dissolution of calcite is determined by the overall reaction



We test now the assumption that this change is responsible for the observed conductivity change. To check our assumption, we analyzed the changes of the concentration of Ca²⁺ (the main cations in the pore water) by ionic chromatography at different saturations (Figure 5). The initial calcium

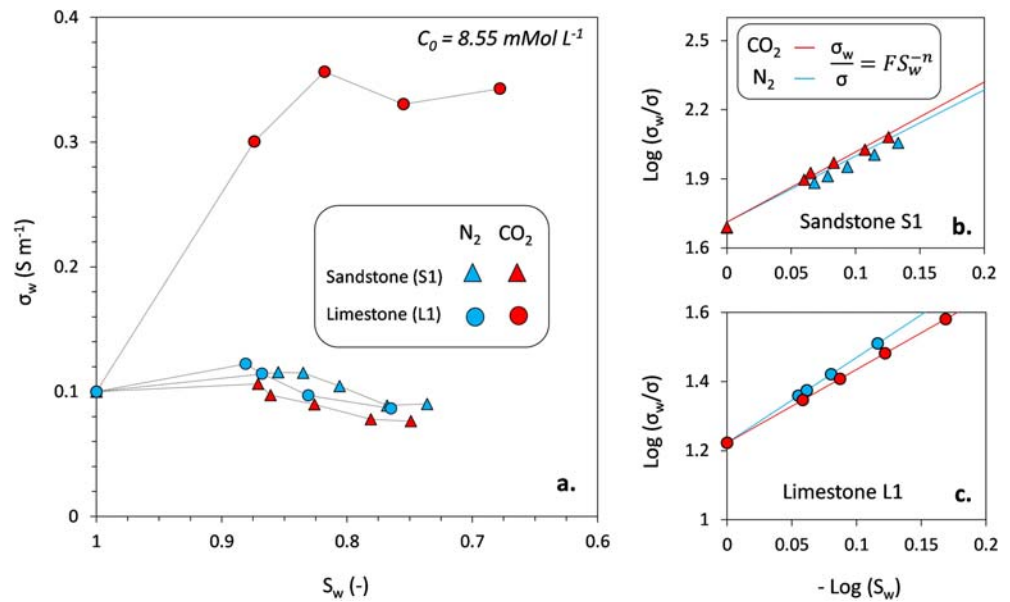


Figure 7. Pore water conductivity during the drainage (a) under CO₂ (red symbols) and N₂ (blue symbols) conditions, calculated using equation (7), for the limestone L1 (circles) and the sandstone S1 (triangles). The initial NaCl brine concentration is 8.55 mMol/L. (b, c) Rock conductivity dependence of pore water conductivity for the sandstone S1 (upper graph) and the limestone L1 (lower graph). Models (blue and red lines) are calculated using equation (5).

content (at $S_w = 1$) is about 10 mg/L (when the brine is equilibrated with the surface of the rock), whereas its final concentration (during drainage) is close to 350 mg/L. This is 40 times higher than the initial concentration. The Ca²⁺ equilibrium in the pore water is reached at the end of the second desaturation step ($S_w \approx 0.863$). At the same time, the electrical rock conductivity reaches its higher value during this drainage step (Figure 5a). When the Ca²⁺ equilibrium is reached, the conductivity decreases with decreasing the saturation following the second Archie's law (Figure 5c). This result is not however consistent with the studies of Dreybrodt et al. (1997) and Lide (2003), which argue that

conductivity modifications in pore water are mostly related to CO₂ dissociation in water than calcite dissolution due to the high value of gas dissolution kinetic of CO₂ for the first ones, and due to the higher value of H⁺ ionic conductivity than Ca²⁺ ionic conductivity for the second one.

In order to go one step further in our analysis, we performed a numerical simulation test with the software package PHREEQC (Parkhurst & Appelo, 1999). We use this software to estimate the evolution of the overall dissolution reactions in the sandstone S1 and the limestones L2, using experimental CO₂ partial pressures and brine NaCl concentration (Figure 6). As expected from equation (17), the CO₂ dissolution in pore water (equation (17)) is the only reason of the presence of HCO₃⁻ in the pore fluid (Figure 6a). Note that the negligible concentration of CO₃²⁻ (equation (17)) is explained by the low value of the pH during drainage (Figure 6c). The presence of HCO₃⁻ and H⁺ have a low impact on the overall ionic strength of the pore fluid (HCO₃⁻: 0.6%; H⁺: 0.6%; Na⁺: 49.4%; Cl⁻: 49.6%).

At the opposite, the overall reaction leading to the dissolution of calcite in presence of CO₂ lead to high concentrations of Ca²⁺ and HCO₃⁻ with respect to what is expected from equation (21) in the pore fluid

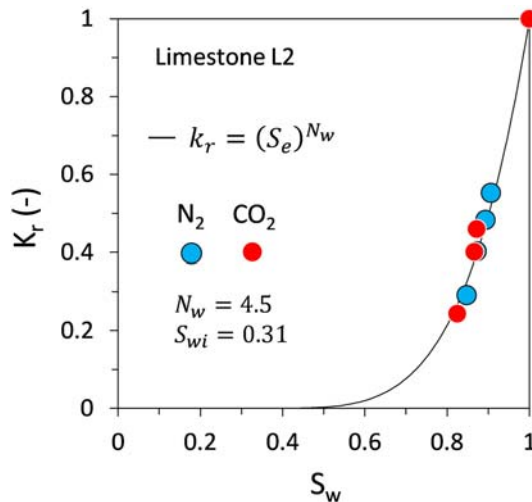


Figure 8. Water relative permeability data during drainage using N₂ (blue circles) and CO₂ (red circles) for the limestone L2. In each case, the Corey exponent (N_w) is equal to 4.5 and determined using the least squares method.

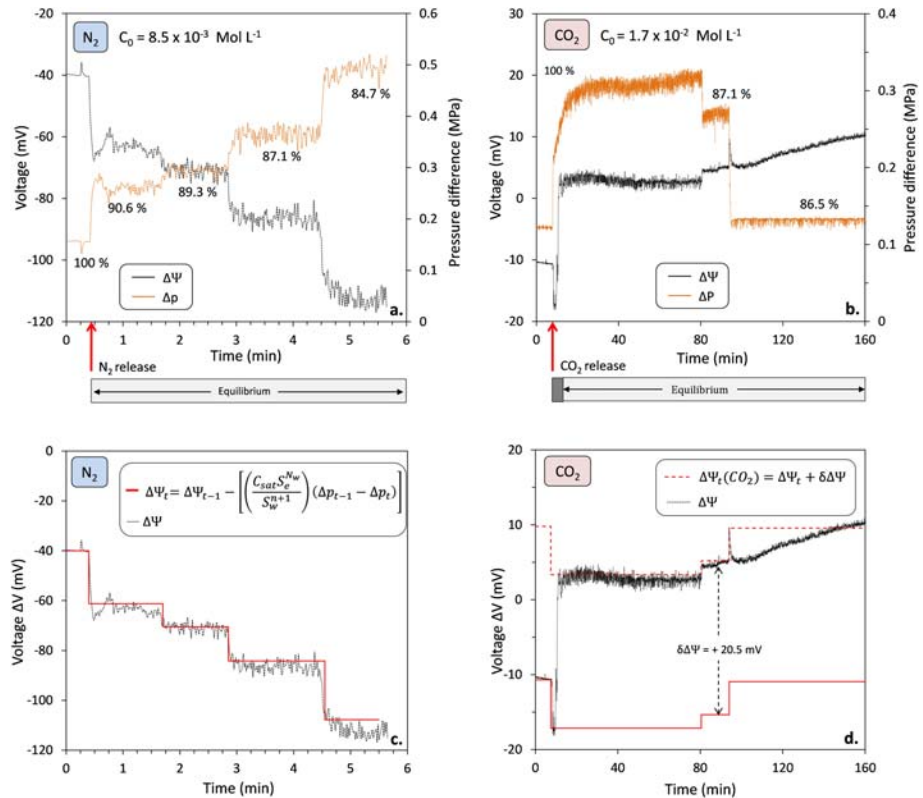


Figure 9. Streaming potential during drainage in the limestone L2. (a, b) Voltage (black line) and pressure difference (orange line) relationships in a brine-N₂ (a) and a brine-CO₂ (b) system, for different saturation steps at NaCl brine concentrations, respectively, equal to 8.55 mMol/L and 17.1 mMol/L. (c, d) Voltage during the drainage associated to the theoretical voltage calculated using equation (24) (red line) under (c) N₂ and (d) CO₂ conditions. The red dashed line represents the theoretical model based on equations (10), (14), and (15). The potential difference $\delta\Delta\psi$ between the two models is equal to 20.5 mV.

(Figure 6b). The simulation seems applicable to our system. Data (obtained using ionic chromatography) and simulated value of Ca²⁺ dissolution are consistent in the limestone L2 (Figure 6b). Ca²⁺ and HCO₃⁻ have a high impact on the overall ionic strength of the pore fluid (Ca²⁺: 46.2%; HCO₃⁻: 25.0%; H⁺: negligible; Na⁺: 14.4%; Cl⁻: 14.4%). Therefore, the conductivity of pore water is controlled by the calcite dissolution especially by the high contribution of Ca²⁺ on the overall ionic strength of the pore water.

Moreover, the electrical rock conductivity is related to the saturation by equation (5) when the Ca²⁺ equilibrium is reached. At the saturation $S_w \approx 0.863$, we determine the saturation exponent $n = 2.62$. This value of the saturation exponent is close to the value of the saturation determined under nitrogen conditions ($n = 2.30$).

4.2.4. Pore Water Conductivity

In section 4.1, we observe that the porosity does not change in a carbonate-brine system in presence of CO₂, at ambient temperature and with a pore pressure in the range 0.1–0.4 MPa. The formation factor (F) and the saturation exponent (n) remain also the same. The formula proposed by Le Roux et al. (2013) is applicable in our case when surface conductivity can be neglected (see section 4.2.1). We can use this model to calculate and monitor the pore water conductivity (equation (7)) relative to the experiments presented in Figure 4. In presence of N₂ or CO₂, the pore water conductivity is quite the same (we just observe a low decrease of conductivity from 0.1 to 0.08 S/m) during drainage in the sandstone S1 (Figure 7a). With an initial NaCl brine concentration (C_0) equal to 8.55 mMol/L, the initial pore water conductivity is equal to 0.1 S/m at $S_w = 1$, whereas it is also around 0.1 S/m at $S_w = 0.74$ in each case.

For limestone L1, the pore water conductivity is also around 0.1 S/m in presence of N₂ in the saturation range $S_w = 0.75$ –1. This is not the case in presence of CO₂. As shown above (see section 4.2.3) the pore water conductivity is controlled both by the calcite dissolution and the presence of Ca²⁺ in pore water. Its value

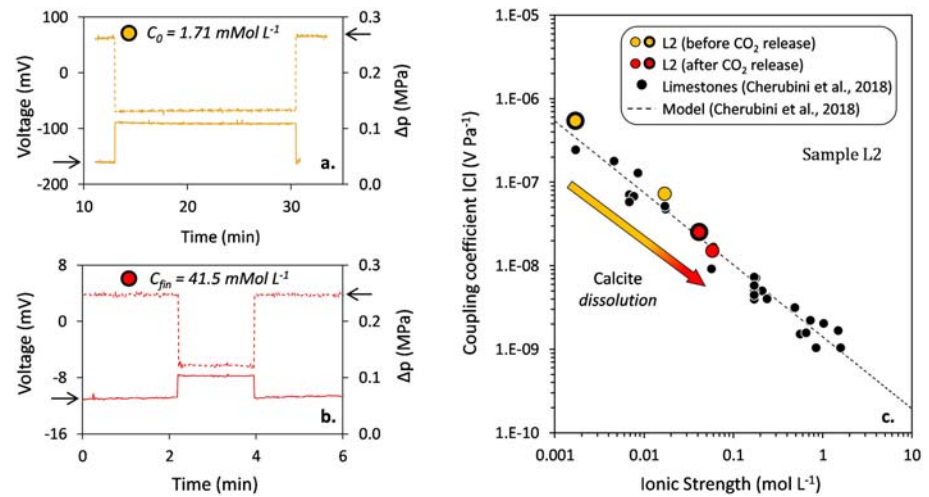


Figure 10. Streaming potential coupling coefficient at full saturation in the limestone L2 (a) before CO₂ release ($C_{\text{sat}} = -5.46 \times 10^{-7}$ V/Pa) and (b) after CO₂ release ($C_{\text{sat}} = -2.55 \times 10^{-8}$ V/Pa). The initial NaCl brine concentration is equal to 1.71 mMol/L, whereas the total ionic strength after dissolution equals 41.5 mMol/L. (c) These results are compared to the absolute values of streaming potential coupling coefficient data (black circles) and model (dashed line) obtained in carbonate rocks by Cherubini et al. (2018), using NaCl brines, at full saturation.

increases in the saturation range 1–0.82 to reach a stable value around 0.34 S/m in the saturation range 0.82–0.67. Then, the rock conductivity is related to the saturation by the same power law in the sandstone S1 (Figure 7b) and in the limestone L1 (Figure 7c), in presence of N₂ or CO₂, adding pore fluid conductivity corrections.

4.3. CO₂ Effects on Electrokinetic Properties

We evaluate now the influence of CO₂ on the streaming potential in porous media. The fitting parameters are the saturation Archie’s exponent (n) and the Corey exponent (N_w), which are both determined using equation (5) (assuming that the surface conductivity is negligible) and water relative permeability curves with drainage data (Figure 8), respectively. These parameters will be used to establish a predictive curve for the streaming potential based on the Helmholtz-Smoluchowski equation (section 4.3.1) and the relative streaming potential coupling coefficient model (equation (15)).

4.3.1. Streaming Potential Model

Drainage processes under N₂ and CO₂ conditions have been performed on the core samples L1 and L2 (Figure 8) to determine their relative permeability (k_r) curves. In turn, these curves are fitted with the relative permeability model ($k_r = S_e^{N_w}$) of Brooks and Corey (1964) and we obtain the same value of the Corey exponent $N_w = 4.5$ for the two core samples. At each saturation step, the voltage and the pressure difference between the inlet and the outlet face are recorded (Figures 9a and 9b). The ratio between the pressure difference and the voltage (in other words, the streaming potential coupling coefficient, see equation (10)) is negative. We focus on streaming potential data under unsaturated conditions in a limestone (L1 with N₂ and L2 with CO₂). We propose to modify equation (10) as

Table 2

Ionic Strength, Streaming Potential Coupling Coefficient (C_{sat}), and Zeta Potential (ζ) of the Saturated Sample L2 for Two Drainage Experiments, Before and After the CO₂ Injection

Sample L2	Ionic strength (mMol/L)		C_{sat} (nV/Pa)		ζ (mV)	
	Before CO ₂	After CO ₂	Before CO ₂	After CO ₂	Before CO ₂	After CO ₂
Drainage 1	1.7	41.5	−546.0	−25.5	−23.9	−18.7
Drainage 2	17.1	58.6	−72.6	−15.0	−22.1	−15.6

Note. The zeta potential is calculated from equation (11).

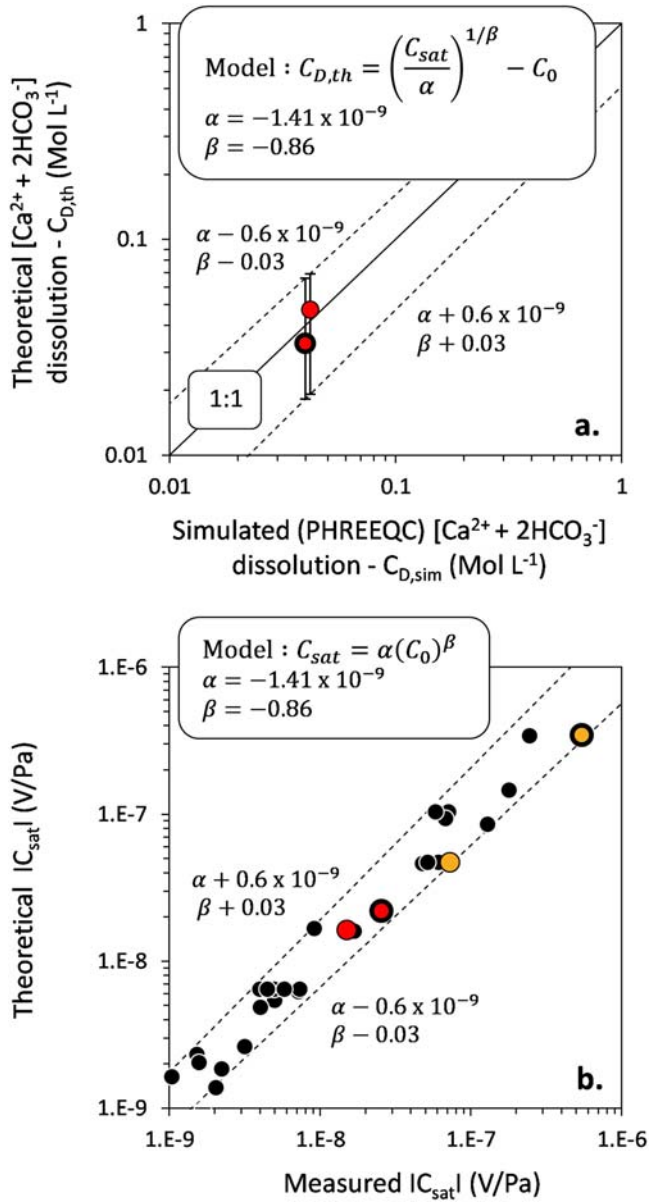


Figure 11. Measured versus theoretical $[Ca^{2+} + 2HCO_3^-]$ dissolution after CO_2 release in the limestone L2. (a) The theoretical dissolution is calculated using equation (26), with $\alpha = -1.41 \times 10^{-9}$ and $\beta = -0.86$ (values from Cherubini et al., 2018). Using two initial NaCl brine concentrations ($C_0 = 1.71$ mMol/L (orange circle, thick border) and $C_0 = 17.1$ mMol/L (orange circle, thin border)), the streaming potential coupling coefficient is respectively equals to $C_{sat} = -25.5$ nV/Pa and $C_{sat} = -15.0$ nV/Pa after CO_2 release. (b) The error bars in the upper figure are determined using the streaming potential coupling coefficient data of Cherubini et al. (2018) with their uncertainty.

strength in carbonates (Cherubini et al., 2018). As expected, the use of CO_2 has a real impact on the value of C_{sat} because of calcite dissolution. Although we lead drainage in carbonates using CO_2 only twice, we saw at a first glance that the streaming potential coupling coefficient could be an interesting tool, alternatively to costly methods to determine the dissolution rate after CO_2 injection in carbonates. By subtracting the initial brine concentration to the final brine concentration after CO_2 release calculated from streaming potential measurements, we obtain,

$$C(S_w) = \left(\frac{\Delta\Psi}{\Delta p}\right)_{J=0} = \frac{\Delta\Psi_{t-1} - \Delta\Psi_t}{\Delta p_{t-1} - \Delta p_t}, \quad (22)$$

$$\Delta\Psi_t = \Delta\Psi_{t-1} - [C(S_w)(\Delta p_{t-1} - \Delta p_t)]. \quad (23)$$

Combining equations (15) and (23) leads to

$$\Delta\Psi_t = \Delta\Psi_{t-1} - \left[\frac{C_{sat} S_e^{N_w}}{S_w^{n+1}} (\Delta p_{t-1} - \Delta p_t)\right]. \quad (24)$$

The streaming potential at a given time $\Delta\Psi_t$ (V) is now connected to the water saturation S_w and the streaming potential coupling coefficient at full saturation C_{sat} . This model is fitted with experimental data in Figures 9c and 9d, under nitrogen and carbon dioxide conditions. On one hand, the model fits quite well with data when the nonpolar phase is nitrogen (red line, Figure 9c). The initial streaming potential ($\Delta\Psi_0$, at $S_w = 1$) is equal to -40 mV for a brine salinity equal to 8.55 mMol/L. On the other hand, the model does not fit with data when carbon dioxide is injected (red line, Figure 9d). The model seems only valid before and few seconds after the CO_2 injection. There is a voltage drop immediately after the injection shown by a significant increase of the observed streaming potential. However, it is possible to translate the model and fit it with data after the CO_2 injection, using a given streaming potential difference $\delta\Delta\Psi$ equal to $+20.5$ mV (red dashed line in Figure 9d) as,

$$\Delta\Psi_t(CO_2) = \Delta\Psi_t + \delta\Delta\Psi. \quad (25)$$

We saw in section 4.2.4 that the pore water conductivity increases after the CO_2 release until it reaches a stable value quickly. This effect probably explains the voltage drop after the injection. The model fits quite well when the pore water is at the equilibrium with the solid phase. That means that the relative streaming potential coupling coefficient model of Revil et al. (2007) is also valid using CO_2 and not only with an inert gas (such as N_2) as tested in Cherubini et al. (2018).

4.3.2. Influence of Calcite Dissolution on C_{sat}

The streaming potential coupling coefficient has been calculated before and after CO_2 release during two drainage experiments on the sample L2 (Figure 10). Its magnitude decreases from -546.0 to -25.5 nV/Pa and from -72.6 to -15.0 nV/Pa when the initial brine concentrations are respectively equal to 1.7 and 17.1 mMol/L (Table 2). The initial brine concentration is known (brine prepared in laboratory), whereas the final concentration has been determined using ionic chromatography and PHREEQC. Initial (yellow circles) and final (red circles) data of the streaming potential coupling coefficient (at $S_w = 1$) are represented in Figure 10c and are closed to the trend connecting C_{sat} and the ionic

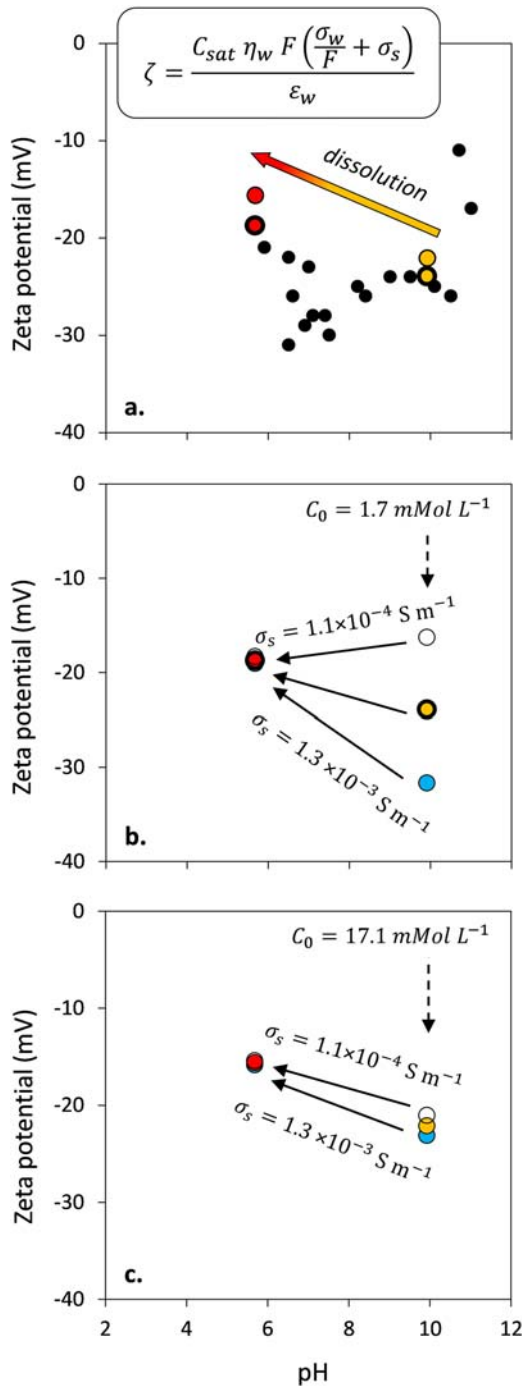


Figure 12. Variations of the zeta potential as a function of pH. (a) Our data are presented in colored circles showing the influence of dissolution on the magnitude of the zeta potential. Data of Guichet et al. (2006) are also represented (black circles) at constant ionic strength of the aqueous solution (2.0×10^{-3} Mol/L) using a CaCl_2 electrolyte. Their measurements were performed with a sand composed of 98% of quartz and 2% of calcite. (b, c) Check of the sensitiveness of zeta potential for various surface conductivities in the pH range 5.5–10 for initial brine concentrations (C_0) equal to 1.7 and 17.1 mMol/L^{−1} respectively. The values of 1.1×10^{-4} S/m is taken from Guichet et al. (2006), whereas the value of 1.3×10^{-3} S/m is from Li et al. (2016). Note that the surface conductivity of our sample L2 before drainage (orange circle) is equal to 7.0×10^{-4} S/m.

$$C_{D,\text{th}} = \left(\frac{C_{\text{sat}}}{\alpha} \right)^{1/\beta} - C_0, \quad (26)$$

with C_0 (Mol/L) the initial brine concentration and $C_{D,\text{th}}$ (Mol/L) the theoretical dissolution rate calculated from streaming potential measurements. The fitting parameters $\alpha = -(1.41 \pm 0.60) \times 10^{-9}$ and $\beta = -0.86 \pm 0.03$ are defined from the study of Cherubini et al. (2018) (see Figure 11b). The dissolution rate is in the same range in spite of the initial brine concentration ($C_{D,\text{th}} = 42$ mMol/L and $C_{D,\text{th}} = 40$ mMol/L for $C_0 = 17.1$ mMol/L and $C_0 = 1.7$ mMol/L, respectively). In both cases, the theoretical dissolution rate calculated from streaming potential measurements is in the same range as the values obtained using PHREEQC (Figure 11a).

4.3.3. Zeta Potential on the Calcite-Water Interface

The zeta potential calculated from streaming potential coupling coefficient data (equation (11)) presents a decrease in magnitude after dissolution, when the ionic strength increases (Table 2) in both drainage cases. The magnitude of the zeta potential decreases from -23.9 to -18.7 mV with an initial brine concentration of 1.7 mMol/L and from -22.1 to -15.6 mV for an initial concentration equal to 17.1 mMol/L. This decrease in magnitude was expected for limestones (Cherubini et al., 2018; Li et al., 2016). Indeed, it is expected to increase with the pH in the pH range 5.5–10 (Figure 12a). However, it is complicated to dissociate the effects of pH and ionic strength on the zeta potential magnitude. Li et al. (2016) showed a slight decrease of the zeta potential magnitude at constant brine concentration, assuming that the influence of the calcite dissolution is negligible under atmospheric CO_2 partial pressure conditions ($p_{\text{CO}_2} = 10^{-1.43}$ kPa). We question this assumption using PHREEQC. Indeed, at $p_{\text{CO}_2} = 10^{-1.43}$ kPa, the ionic strength of the dissolution term [$\text{Ca}^{2+} + 2\text{HCO}_3^-$] is equal to 1.5 mMol/L, which represents 60% of the total ionic strength of the aqueous solution (2.5 mMol/L) when the initial NaCl concentration is equal to 1.0 mMol/L, hence the need to store the aqueous solutions in glassware to avoid equilibrating chemical processes with atmospheric components (particularly the CO_2). In comparison, Guichet et al. (2006) showed a quite stable zeta potential (however with a significant data dispersion) in the pH range 5.5–10 (Figure 12a) on a silica sand containing 2% of calcite.

Guichet et al. (2006) measured scattered zeta potential values for pH higher than 10.5 and assumed that this scattering is related to calcite precipitation (Figure 12a). As seen previously in this study and in Li et al. (2016) this scattering does not seem to be due to the calcite-water interface, but from the decrease in permeability, as they suggested. This assumption is consistent with the following equation obtained by combining equations (11) and (13), as

$$\zeta = -\frac{k\hat{Q}_v F}{\epsilon_w}. \quad (27)$$

However, they performed their experiments on a sand characterized by a very low value of the surface conductivity ($\sigma_s = 1.1 \times 10^{-4}$ S/m) using a CaCl_2 electrolyte with a concentration equal to 2.0×10^{-3} Mol/L. We represent the values of the zeta potential of the sample L2 assuming surface conductivity variations (Figures 12b and 12c). We take the values of $\sigma_s = 1.1 \times 10^{-4}$ S/m (Guichet et al., 2006; represented by the white

circles) and $\sigma_s = 1.3 \times 10^{-3}$ S/m (Li et al., 2016; represented by the blue circles) for initial brine concentrations equal to 1.7×10^{-3} Mol/L (Figure 12b) and 17.1×10^{-3} Mol. L (Figure 12c). For low concentrations (Figure 12b), the magnitude of the zeta potential is highly influenced by the surface conductivity effects, while this is not the case for higher salinities (Figure 12c). This phenomenon could explain the scattered zeta potential values measured by Guichet et al. (2006) because of the likely decrease of the electrolyte concentration due to calcite precipitation at high pH values (>10.5).

5. Conclusion

Electrical and electrokinetic measurements were performed to investigate the impact of CO₂ during drainage in carbonate rocks. Electrical conductivity measurements are also performed during drainage with N₂ (considered as a neutral gas) and CO₂ in a sandstone (considered as a chemically neutral rock with respect to CO₂) and limestones (reactive rocks).

In a pure limestone, the rock conductivity increases when the saturation decreases until the pore water equilibrium is reached, when the nonwetting phase is composed of CO₂. The pore water conductivity does not vary during drainage in a pure sandstone whatever the nonwetting phase (N₂ or CO₂). This assumption is also true in a limestone in presence of N₂ only. The presence of CO₂ has a drastic impact regarding the conductivity of the pore water. Two main phenomena are tested to explain this increase of pore water conductivity in presence of CO₂ in carbonates. The change in Ca²⁺ in the pore water during drainage with CO₂ in a limestone explains the change in the pore water conductivity. Indeed, the ionic strength of water is dominated by the presence of Ca²⁺ when calcite dissolution occurred.

Electrokinetics properties are also impacted by the presence of CO₂ in carbonates. The dissolution of calcite after a CO₂ release leads to a decrease of the magnitude of the streaming potential coupling coefficient due to the increase of the water ionic strength (and thereby the increase of brine conductivity) in agreement with the prediction of the Helmholtz-Smoluchowski theory. The streaming potential coupling coefficient seems to be a potentially interesting tool to estimate brine concentrations after a CO₂ release in carbonates, and thereby, a tool to estimate dissolution rates. Moreover, we can expect to use this parameter in order to detect CO₂ leakages from storage sites.

Acknowledgments

This research has been supported by IFP Energies Nouvelles, Rueil-Malmaison, France. The contribution of A. Revil is supported by the University of Melbourne through a project funded by the Commonwealth of Australia (Contract CR-2016-UNIV. MELBOURNE-147672-UMR5275). We also thank Anélia Petit from ENSEGID and Claire Lix from IFPEN for their time. Per AGU's Data Policy, the supporting information data have been deposited in a general repository under the reference <https://doi.org/10.13140/RG.2.2.32988.54403>. We thank the three referees and the Editor for their comments.

References

- Alroudhan, A., Vinogradov, J., & Jackson, M. D. (2016). Zeta potential of intact natural limestone: Impact of potential-determining ions Ca, Mg and SO₄. *Colloids and Surfaces A: Physicochemical and Engineering Aspects*, 493, 83–98. <https://doi.org/10.1016/j.colsurfa.2015.11.068>
- Archie, G. E. (1942). The electrical resistivity log as an aid in determining some reservoir characteristics. *Transactions of the American Institute of Mining and Metallurgical Engineers*, 146(01), 54–62. <https://doi.org/10.2118/942054-G>
- Aubert, M., & Yéné Atanga, Q. (1996). Self-potential method in hydrogeological exploration of volcanic areas. *Groundwater*, 34(6), 1010–1016. <https://doi.org/10.1111/j.1745-6584.1996.tb02166.x>
- Auffray, B., Garcia, B., Lienemann, C. P., Sorbier, L., & Cerepi, A. (2016). Zn (II), Mn (II) and Sr (II) behavior in a natural carbonate reservoir system. Part II: Impact of geological CO₂ storage conditions. *Oil & Gas Science and Technology*, 71, 48. <https://doi.org/10.2516/ogst/2015043>
- Bachu, S., Gunter, W. D., & Perkins, E. H. (1994). Aquifer disposal of CO₂—Hydrodynamic and mineral trapping. *Energy Conversion and Management*, 35(4), 269–279. [https://doi.org/10.1016/0196-8904\(94\)90060-4](https://doi.org/10.1016/0196-8904(94)90060-4)
- Benson, S. M., & Cole, D. R. (2008). CO₂ sequestration in deep sedimentary formations. *Elements*, 4(5), 325–331. <https://doi.org/10.2113/gselements.4.5.325>
- Brooks, R. H., & Corey, A. T. (1964). Hydraulic properties of porous media. *Hydrology Papers*, 3, Colorado State University.
- Cerepi, A., Cherubini, A., Garcia, B., Deschamps, H., & Revil, A. (2017). Streaming potential coupling coefficient in unsaturated carbonate rocks. *Geophysical Journal International*, 210(1), 291–302. <https://doi.org/10.1093/gji/ggx162>
- Cherubini, A., Garcia, B., Cerepi, A., & Revil, A. (2018). Streaming potential coupling coefficient and transport properties of unsaturated carbonate rocks. *Vadose Zone Journal*, 17(1), 180030. <https://doi.org/10.2136/vzj2018.02.0030>
- Cohen, G., Loisy, C., Laveuf, C., Le Roux, O., Delaplace, P., Magnier, C., et al. (2013). The CO₂-Vadose project: Experimental study and modelling of CO₂ induced leakage and tracers associated in the carbonate vadose zone. *International Journal of Greenhouse Gas Control*, 14, 128–140. <https://doi.org/10.1016/j.ijggc.2013.01.008>
- Corwin, R. F., & Hoover, D. B. (1979). The self-potential method in geothermal exploration. *Geophysics*, 44(2), 226–245. <https://doi.org/10.1190/1.1440964>
- Darnet, M., Marquis, G., & Sailhac, P. (2003). Estimating aquifer hydraulic properties from the inversion of surface streaming potential (SP) anomalies. *Geophysical Research Letters*, 30(13), 1679. <https://doi.org/10.1029/2003GL017631>
- Dreybrodt, W., Eisenlohr, L., Madry, B., & Ringer, S. (1997). Precipitation kinetics of calcite in the system CaCO₃-H₂O-CO₂: The conversion to CO₂ by the slow process H⁺+HCO₃⁻ → CO₂+H₂O as a rate limiting step. *Geochimica et Cosmochimica Acta*, 61(18), 3897–3904. [https://doi.org/10.1016/S0016-7037\(97\)00201-9](https://doi.org/10.1016/S0016-7037(97)00201-9)

- Dukhin, S. S., & Derjaguin, B. V. (1974). Electrokinetic phenomena. *Surface and Colloid Science*, 7, 322.
- Enick, R. M., & Klara, S. M. (1990). CO₂ solubility in water and brine under reservoir conditions. *Chemical Engineering Communications*, 90(1), 23–33. <https://doi.org/10.1080/00986449008940574>
- Garcia, B., Delaplace, P., Rouchon, V., Magnier, C., Loisy, C., Cohen, G., et al. (2013). The CO₂-Vadose project: Numerical modelling to perform a geochemical monitoring methodology in the vadose zone. *International Journal of Greenhouse Gas Control*, 14, 247–258. <https://doi.org/10.1016/j.ijggc.2013.01.029>
- Giese, R., Henningses, J., Lüth, S., Morozovaa, D., Schmidt-Hattenberger, C., Würdemann, H., et al. (2009). Monitoring at the CO₂SINK site: A concept integrating geophysics, geochemistry and microbiology. *Energy Procedia*, 1(1), 2251–2259. <https://doi.org/10.1016/j.egypro.2009.01.293>
- Grigg, R. B., McPherson, B. J., & Svec, R. K. (2003). Laboratory and model tests at reservoir conditions for CO₂-brine-carbonate rock systems interactions. Paper presented at 2nd Annual Carbon Sequestration Conference, Alexandria, Egypt.
- Guichet, X., Jouniaux, L., & Catel, N. (2006). Modification of streaming potential by precipitation of calcite in a sand-water system: Laboratory measurements in the pH range from 4 to 12. *Geophysical Journal International*, 166(1), 445–460. <https://doi.org/10.1111/j.1365-246X.2006.02922.x>
- Helmholtz, H. (1879). Studien über elektrische Grenzschichten. *Annalen der Physik*, 7, 337–382.
- Hunter, R. J. (1981). *Zeta Potential in Colloid Science*. New York: Academic.
- Jackson, M. D. (2010). Multiphase electrokinetic coupling: Insights into the impact of fluid and charge distribution at the pore scale from a bundle of capillary tubes model. *Journal of Geophysical Research*, 115, B07206. <https://doi.org/10.1029/2009JB007092>
- Jenkins, C. R., Cook, P. J., Ennis-King, J., Undershultz, J., Boreham, C., Dance, T., et al. (2012). *Proceedings of the National Academy of Sciences of the United States of America*, 109(2), E35–E41. <https://doi.org/10.1073/pnas.1107255108>
- Jougnot, D., Linde, N., Revil, A., & Doussan, C. (2012). Derivation of soil-specific streaming potential electrical parameters from hydrodynamic characteristics of partially saturated soils. *Vadose Zone Journal*, 11(1). <https://doi.org/10.2136/vzj2011.0086>
- Kiessling, D., Schmidt-Hattenberger, C., Schuett, H., Schilling, F., Krueger, K., Schoebel, B., et al. (2010). Geoelectrical methods for monitoring geological CO₂ storage: First results from cross-hole and surface-downhole measurements from the CO₂SINK test site at Ketzin (Germany). *International Journal of Greenhouse Gas Control*, 4(5), 816–826. <https://doi.org/10.1016/j.ijggc.2010.05.001>
- Le Roux, O., Cohen, G., Loisy, C., Laveuf, C., Delaplace, P., Magnier, C., et al. (2013). The CO₂ Vadose project: Time lapse geoelectrical monitoring during CO₂ diffusion in the carbonate vadose zone. *International Journal of Greenhouse Gas Control*, 16, 156–166. <https://doi.org/10.1016/j.ijggc.2013.03.016>
- Lewicki, J. L., Oldenburg, C. M., Dobeck, L., & Spangler, L. (2007). Surface CO₂ leakage during two shallow subsurface CO₂ releases. *Geophysical Research Letters*, 34, L24402. <https://doi.org/10.1029/2007GL032047>
- Li, S., Leroy, P., Heberling, F., Devau, N., Jougnot, D., & Chiaberge, C. (2016). Influence of surface conductivity on the apparent zeta potential of calcite. *Journal of Colloid and Interface Science*, 468, 262–275. <https://doi.org/10.1016/j.jcis.2016.01.075>
- Lide, D. R. (2003). *Handbook of Chemistry and Physics*, (84th ed.). Boca Raton, Florida: CRC Press.
- Linde, N., Jougnot, D., Revil, A., Matthäi, S. K., Arora, T., Renard, D., & Doussan, C. (2007). Streaming current generation in two-phase flow conditions. *Geophysical Research Letters*, 34, L03306. <https://doi.org/10.1029/2006GL028878>
- Lindsay, W. L. (1979). *Chemical equilibria in soils*. New York: Wiley.
- Liu, N., Liu, L., Qu, X., Yang, H., Wang, L., & Zhao, S. (2011). Genesis of authigenic carbonate minerals in the Upper Cretaceous reservoir, Honggang Anticline, Songliao Basin: A natural analog for mineral trapping of natural CO₂ storage. *Sedimentary Geology*, 237(3–4), 166–178. <https://doi.org/10.1016/j.sedgeo.2011.02.012>
- Loisy, C., Cohen, G., Laveuf, C., le Roux, O., Delaplace, P., Magnier, C., et al. (2013). The CO₂-Vadose project: Dynamics of the natural CO₂ in a carbonate vadose zone. *International Journal of Greenhouse Gas Control*, 14, 97–112. <https://doi.org/10.1016/j.ijggc.2012.12.017>
- Luquot, L., & Gouze, P. (2009). Experimental determination of porosity and permeability changes induced by injection of CO₂ into carbonate rocks. *Chemical Geology*, 265(1–2), 148–159. <https://doi.org/10.1016/j.chemgeo.2009.03.028>
- Moore, J. R., Glaser, S. D., & Frank Morrison, H. (2004). The streaming potential of liquid carbon dioxide in Berea sandstone. *Geophysical Research Letters*, 31, L17610. <https://doi.org/10.1029/2004GL020774>
- Naudet, V., Revil, A., Bottero, J.-Y., & Bégassat, P. (2003). Relationship between self-potential (SP) signals and redox conditions in contaminated groundwater. *Geophysical Research Letters*, 30(21), 2091. <https://doi.org/10.1029/2003GL018096>
- Naudet, V., Revil, A., Rizzo, E., Bottero, J.-Y., & Bégassat, P. (2004). Groundwater redox conditions and conductivity in a contaminant plume from geoelectrical investigations. *Hydrology and Earth System Sciences*, 8(1), 8–22. <https://doi.org/10.5194/hess-8-8-2004>
- Overbeek, J. T. G. (1952). Electrochemistry of the electrical double layer. In H. R. Kruyt (Ed.), *Colloids Science*, (Vol. 1, pp. 115–193). Amsterdam - Houston - New York - London: Elsevier Publ. Co.
- Parkhurst, D. L., & Appelo, C. A. J. (1999). User's guide to PHREEQC (Version 2): A computer program for speciation, batch-reaction, one-dimensional transport, and inverse geochemical calculations. *Water-Resources Investigations Report*, 99-4259. <https://doi.org/10.3133/wri994259>
- Perrier, F., & Morat, P. (2000). Characterization of electrical daily variations induced by capillary flow in the non-saturated zone. *Pure and Applied Geophysics*, 157(5), 785–810. <https://doi.org/10.1007/PL00001118>
- Plummer, L. N., Parkhurst, D. L., & Wigley, T. M. L. (1979). Critical review of the kinetics of calcite dissolution and precipitation. In E. A. Jenne (Ed.), *Chemical modeling in aqueous systems, Symposium series*, (Vol. 93, pp. 537–573). Washington, American Chemical Society. <https://doi.org/10.1021/bk-1979-0093.ch025>
- Rasmuson, A., Gimmi, T., & Flühler, H. (1990). Modeling reactive gas uptake, transport, and transformation in aggregated soils. *Soil Science Society of America Journal*, 54(5), 1206–1213. <https://doi.org/10.2136/sssaj1990.03615995005400050002x>
- Revil, A., & Cerepi, A. (2004). Streaming potentials in two-phase flow conditions. *Geophysical Research Letters*, 31, L11605. <https://doi.org/10.1029/2004GL020140>
- Revil, A., Finizola, A., Sortino, F., & Ripepe, M. (2004). Geophysical investigations at Stromboli volcano, Italy. Implications for ground water flow and paroxysmal activity. *Geophysical Journal International*, 157(1), 426–440. <https://doi.org/10.1111/j.1365-246X.2004.02181.x>
- Revil, A., Kessouri, P., & Torres-Verdín, C. (2014). Electrical conductivity, induced polarization, and permeability of the Fontainebleau sandstone. *Geophysics*, 79(5), D301–D318. <https://doi.org/10.1190/geo2014-0036.1>
- Revil, A., Linde, N., Cerepi, A., Jougnot, D., Matthäi, S., & Finsterle, S. (2007). Electrokinetic coupling in unsaturated porous media. *Journal of Colloid and Interface Science*, 313(1), 315–327. <https://doi.org/10.1016/j.jcis.2007.03.037>
- Revil, A., Pezard, P. A., & Glover, P. W. J. (1999). Streaming potential in porous media: 1. Theory of the zeta potential. *Journal of Geophysical Research*, 104(B9), 20021–20031. <https://doi.org/10.1029/1999JB900089>

- Rosenbauer, R. J., Koksalan, T., & Palandri, J. L. (2005). Experimental investigation of CO₂-brine-rock interactions at elevated temperature and pressure: Implications for CO₂ sequestration in deep-saline aquifers. *Fuel Processing Technology*, 86(14-15), 1581–1597. <https://doi.org/10.1016/j.fuproc.2005.01.011>
- Schmidt-Hattenberger, C., Bergmann, P., Kießling, D., Krüger, K., Rücker, C., Schütt, H., & Ketzin Group (2011). Application of a vertical electrical resistivity array (VERA) for monitoring CO₂ migration at the Ketzin site: First performance evaluation. *Energy Procedia*, 4, 3363–3370. <https://doi.org/10.1016/j.egypro.2011.02.258>
- Shi, J. Q., & Durucan, S. (2005). CO₂ storage in deep unminable coal seams. *Oil & Gas Science and Technology*, 60(3), 547–558. <https://doi.org/10.2516/ogst:2005037>
- Soueid Ahmed, A., Jardani, A., Revil, A., & Dupont, J. P. (2016). Specific storage and hydraulic conductivity tomography through the joint inversion of hydraulic heads and self-potential data. *Advances in Water Resources*, 89, 80–90. <https://doi.org/10.1016/j.advwatres.2016.01.006>
- Strazisar, B. R., Wells, A. W., Rodney Diehl, J., Hammack, R. W., & Veloski, G. A. (2009). Near-surface monitoring for the ZERT shallow CO₂ injection project. *International Journal of Greenhouse Gas Control*, 3(6), 736–744. <https://doi.org/10.1016/j.ijggc.2009.07.005>
- Talman, S. J., Wiwchar, B., Gunter, W. D., & Scarge, C. M. (1990). Dissolution kinetics of calcite in the H₂O-CO₂ system along the steam saturation curve to 210°C. In R. J. Spencer, & I. M. Chou (Eds.), *Fluid-mineral interactions: A tribute to H. P. Eugster*, Geochemical Society Special Publication, (Vol. 2, pp. 41–55).
- Waxman, M. H., & Smits, L. J. M. (1968). Electrical conductivities in oil-bearing shaly sands. *Society of Petroleum Engineers Journal*, 8(02), 107–122. <https://doi.org/10.2118/1863-A>
- Würdemann, H., Möller, F., Kühn, M., Heidug, W., Christensen, N. P., Borm, G., & Schilling, F. R. (2010). CO₂SINK—from site characterization and risk assessment to monitoring and verification. One year of operational experience with the field laboratory for CO₂ storage at Ketzin, Germany. *International Journal of Greenhouse Gas Control*, 4(6), 938–951. <https://doi.org/10.1016/j.ijggc.2010.08.010>
- Zhou, X., Lakkaraju, V. R., Apple, M., Dobeck, L. M., Gullickson, K., Shaw, J. A., et al. (2012). Experimental observation of signature changes in bulk soil electrical conductivity in response to engineered surface CO₂ leakage. *International Journal of Greenhouse Gas Control*, 7, 20–29. <https://doi.org/10.1016/j.ijggc.2011.12.006>